


Ghost diffractive deep neural networks: Optical classifications using light's second-order coherence

Zhiyuan Ye,¹ Chenjie Zhou¹,^{*} Chen-Xin Ding,¹ Jilun Zhao,¹ Shuming Jiao^{1,2}, Hai-Bo Wang,¹ and Jun Xiong^{1,*}

¹Department of Physics, Applied Optics Beijing Area Major Laboratory, Beijing Normal University, 100875 Beijing, China

²Peng Cheng Laboratory, Shenzhen, 518055 Guangdong, China

 (Received 8 May 2023; revised 18 August 2023; accepted 18 October 2023; published 6 November 2023)

Since Hanbury Brown and Twiss proposed intensity interferometry in 1956, light's fluctuating nature, high-order coherence, and spatial correlations have become not only the cornerstones of quantum optics but also resources for many classical optical applications. Correlation-based optical metrologies, including ghost imaging and ghost diffraction, have distinct advantages ranging from local to nonlocal geometry, spatially coherent to incoherent light, and array to single-pixel sampling. In this paper we propose ghost diffractive deep neural networks (GD²NNs), a nonlocal optical information-processing system that combines traditional ghost diffraction with cascaded diffraction layers “learned” with use of diffractive deep neural networks. GD²NNs use light's second-order coherence to enable image-free and interferometer-free coherent beam-demanded phase-object sorting with thermal light. Furthermore, GD²NNs convert the general encoder-decoder-detector cascaded framework into a parallel one, resulting in no optical interaction between the encoder and the decoder. As a proof-of-principle demonstration, we numerically and experimentally classify different phase objects using three-layer and two-layer GD²NNs, respectively. This paper effectively provides a paradigm shift, particularly for diffraction-related coherent linear optical information processing systems, from spatially coherent to incoherent light and from cascaded to parallel processing.

DOI: [10.1103/PhysRevApplied.20.054012](https://doi.org/10.1103/PhysRevApplied.20.054012)

I. INTRODUCTION

The story of ghost diffraction (GD) originates from a counterintuitive two-photon interference experiment by Shih's group [1]: after the preparation of the entangled photon pair through a nonlinear crystal, one photon interacts with a double slit and then is detected by a fixed pinholelike detector in the signal arm; meanwhile, another scanning detector is triggered to synchronously detect its twin photon in the idle arm. Intriguingly, the interference pattern is not visible in the signal arm but is produced in the idle arm with photons that nevertheless do not interact with the double slit at all. The theory behind it as well as the prediction was proposed by Belinskii and Klyshko [2] in 1994 and can be well understood through a geometrical-optics-based picture [3,4] established in 1988, where the *nonlocality* could be conveniently interpreted in terms of advanced waves emitted by one detector toward the other detector replacing the nonlinear crystal with a mirror. Klyshko's advanced-wave picture builds a bridge between coincidence measurement and direct measurement, and

its influence has continued to this day, not only vividly explaining quantum ghost imaging and diffraction but also proving to be fully effective in nonlocal quantum optical information processing. Recent advances include nonlocal aberration cancellation [5], pattern recognition [6,7], and edge enhancement [8,9].

The migration from biphoton to thermal light [10–15] is an ongoing development path in GD modality using classical correlations [16]. For example, Fig. 1(a) shows a typical optical geometry of GD driven by pseudothermal light [17]; it should be noted that thermal light as well as pseudothermal light is typically spatially incoherent light and is thus not destined to produce any coherent diffraction patterns. Such direct measurements rely on the *first-order coherence* (e.g., spatial coherence) of the light source, whereas in GD the measurement of the *second-order coherence* function [18] (or intensity correlation function) in the spatial dimension (the relative time delay τ is by default 0 here),

$$g^{(2)}(\mathbf{r}; \tau = 0) = \frac{\langle I_r(\mathbf{r}_r) I_s(\mathbf{r}_s) \rangle}{\langle I_r(\mathbf{r}_r) \rangle \langle I_s(\mathbf{r}_s) \rangle}, \quad (1)$$

*junixiong@bnu.edu.cn

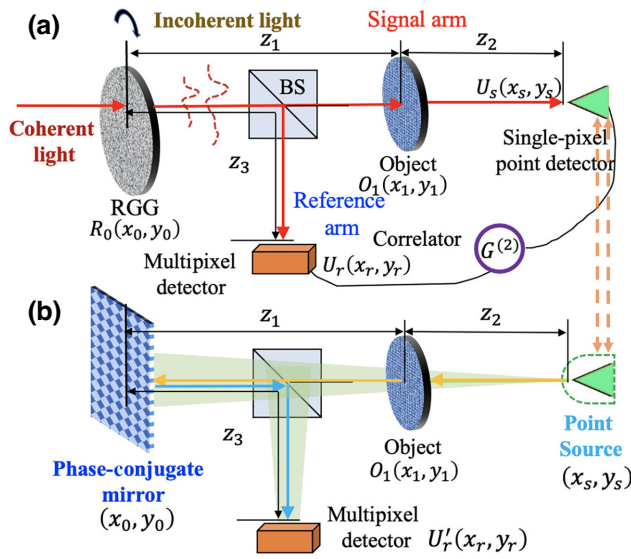


FIG. 1. Geometrical optics of a typical GD setup with pseudothermal light (a) and its unfolded analogy (b). The joint correlation measurement [Eq. (1)], between a point’s intensity fluctuations in the signal arm and spatially resolved all points in the reference arm, enables reconstruction of the object’s diffraction pattern. In (b), according to the phase-conjugate-mirror model [31,32], the advanced wave emitted by the equivalent point source [corresponding to the single-point detector in (a)] is directed to the multipixel detector, where the thermal source in (a) is replaced by a phase-conjugate mirror. BS, beam splitter; RGG, rotating ground-glass plate.

cleverly circumvents this problem and therefore enables the reproduction of the diffraction pattern (see also two examples of coherent imaging of a phase object [19] and Gabor’s holography [20] with spatially incoherent light). Such ideas date back to the Siegert relation [21, 22] ($g^{(2)}(\tau) = 1 + |g^{(1)}(\tau)|^2$) in World War II and, of course, the well-known intensity interferometer demonstrated by Hanbury Brown and Twiss in 1956 [23,24]. The second-order correlation coefficient, $g^{(2)}(0)$, can not only classify light sources (e.g., see two recent examples [25,26]) but can also reflect the correlation strength, generally $g^{(2)}(0) \approx 1$ being uncorrelated and $g^{(2)}(0) > 1$ embodying a bunching effect and correlated as well. To this day, it is concluded that high-order correlations have some generalization advantages; for example, temporal interference beyond coherence time [27], high-speed signal imaging using a slow detector [28], and even super-resolution [29,30], with an inevitable trade-off where the measure of $g^{(2)}$ is essentially the result of an ensemble average shown as “ $\langle \cdot \rangle$ ” in Eq. (1), and therefore requires a large number of realizations.

As a classical counterpart to Klyshko’s advanced-wave picture, the phase-conjugate-mirror model, proposed by Cao *et al.* [31] and experimentally confirmed by Scarcelli

et al. [32], acts as an intermediary between indirect second-order correlation and direct first-order measurement by replacing the thermal source with a phase-conjugate mirror as shown in Fig. 1(b). In this sense, an invisibility cloak [33,34] can be implemented in an unbalanced interferometer with chaotic light. In addition, almost all efforts have been focused on enhancing the performance of GD [35–40]; for example, Vinu *et al.* [39] expanded GD to holographic microscopy. However, to the best of our knowledge, no one instance has demonstrated the possible applicability of GD in coherent optical information processing.

Recently, there has been the development of diffractive deep neural networks (D²NNs) [41–49] that use well-trained cascaded diffractive optical elements (DOEs), similarly to volume holography [50–53], to implement diverse coherent optical applications [54–62]. A D²NN-based optical classification scheme, for example, converts diffracted light of different classes of objects into separate components in a specific degree of freedom of light, such as spatial position (or mode) [41] and spectrum [48]. Differently from image classification based on electrical neural networks [63–65] as shown in Fig. 2(a), D²NNs achieve *all-optical* classification (except for the photoelectric detection end) by comparing the *energy distribution* of different components; see Fig. 2(b). However, at this moment, a key barrier is that D²NNs place severe requirements on the first-order coherence of the light source. Although temporally incoherent broadband light has been demonstrated to exist in D²NNs [42,48], another type of light source, spatially incoherent light [66], is quite limited and hard to use in experiments, because the complex-valued linear transformation in this case is totally invalid by nature such that the approach fails to perform all-optical information processing on phase targets.

In this paper, we integrate D²NNs with GD to create ghost diffractive deep neural networks (GD²NNs), a *nonlocal* or *parallel* classical coherent optical information processing framework as depicted in Fig. 2(c). We implement a phase-target classification scheme by comparing the second-order-correlation-coefficient distribution on $g^{(2)}(\mathbf{r})$ rather than the first-order energy distribution, allowing spatially incoherent light to drive D²NNs with complex-valued linear transformation. In addition to the need for joint optoelectronic measurements at the detection end, well-trained GD²NNs can achieve all-optical inference in this sense. Furthermore, such a nontrivial parallel structure fundamentally challenges the standard “encoder-decoder-detector” cascade structure, and its potential advantages lie in flexible configuration (the decoder and encoder can be configured in two remote locations) and safety performance (valid only for two-party joint measurement). This work paves the way for the application of second-order coherence—yet as a not-fully-exploited degree of

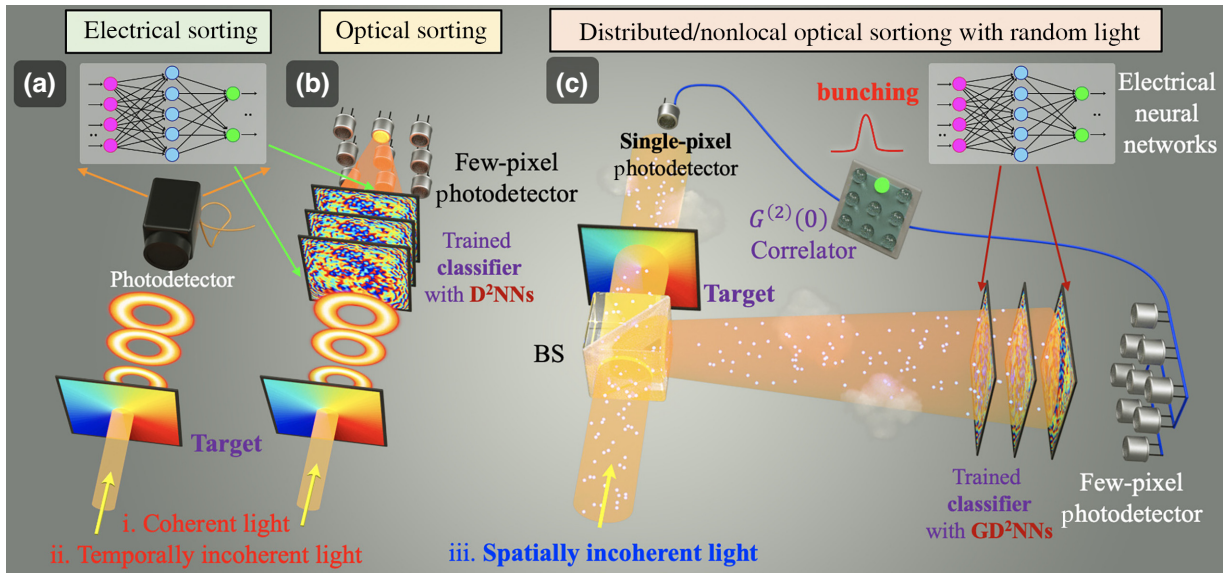


FIG. 2. Three classification schemes. (a) Typical computer-vision framework that first collects optical images and then trains electrical neural networks to complete data-driven pattern recognition; all sorting tasks related to phase targets require spatially coherent illumination. (b) All-optical sorting scheme (D^2NNs) [41] using spatially coherent light and cascaded DOEs, which can be viewed as a classifier or decoder that is well trained by electrical neural networks in advance, and which has a typical “encoder-decoder-detector” structure. After the spatially coherent beam, encoded by the target, passes through the classifier, a distinguishable focus at a specific position will appear on the energy distribution of the few-pixel detection plane, and such an optimization task can be performed by optimizing tens of thousands of diffraction units (optical neurons) through the back-propagation algorithm. (c) Nonlocal or parallel optical sorting scheme (GD^2NNs) driven by spatially incoherent light proposed in this work—The term “nonlocal” or “parallel” denotes that the photons interacting with the target do not interact with the classifier at all, indicating that the target and the classifier are optically interaction-free and thus can be placed in two remote locations; neither piece of single-arm information can complete the optical sorting task due to the source’s chaotic spatial modes (i.e., first-order coherence), but a bunching peak (i.e., $g^{(2)}(\mathbf{r}) > 1$) will recur in the specific position of the second-order coherence function via the joint correlation measurement between the two arms.

freedom of light—to complex coherent optical information processing.

This paper is organized as follows: Sec. II introduces the principles of GD as well as the phase-conjugate-mirror model in the manner of Fourier optics, and revisits GD experiments of pure phase targets to illustrate how to retrieve the target’s coherent diffraction pattern using pseudothermal light. Section III introduces the principle of and training methods for GD^2NNs in a matrixwise manner and presents a numerical and an experimental case, respectively, to classify pure phase targets. Section IV discusses other expansion schemes, potential advantages (or trade-offs), and differences between GD^2NNs and ghost-imaging-based classification schemes.

II. SEEING WITH GD

A. Principle of GD

Generally, GD enables the reconstruction of the diffraction pattern of an object using chaotic light. Figure 1(a) shows a classical GD setup, in which pseudothermal light is generated by a laser to illuminate a rotating ground-glass plate [17]. Then, a beam splitter divides the source into signal and reference arms: the beam in the signal arm

interacts with the object directly but only point information can be accessed by a single-pixel detector, while the beam in the reference arm is directly recorded by a multipixel detector, i.e., the image sensor array. Neither can retrieve the diffraction pattern alone unless the second-order correlation function between the two is retrieved. From the perspective of geometrical optics, such a result of joint correlation measurement can be well interpreted by replacing the thermal source in Fig. 1(a) with a phase-conjugate mirror [31,32] as shown in Fig. 1(b): the single-pixel point detector in Fig. 1(a) acts like a point source emitting a spatially coherent beam toward the multipixel detector.

Here we provide a brief theoretical derivation of this interpretation. According to Fourier optics [67], the optical field’s complex functions in the signal and reference arms in Fig. 1(a) can be expressed, respectively, as

$$\begin{aligned}
 U_s(x_s, y_s) &= \iiint U_0 R_0(x_0, y_0) \Gamma_1(x_1, x_0, y_1, y_0, z_1) \\
 &\quad \times O_1(x_1, y_1) \Gamma_2(x_s, x_1, y_s, y_1, z_2) dx_0 dy_0 dx_1 dy_1, \\
 U_r(x_r, y_r) &= \iint U_0 R_0(x_0, y_0) \Gamma_3(x_r, x_0, y_r, y_0, z_3) dx_0 dy_0,
 \end{aligned} \tag{2}$$

where $U_0(x_0, y_0)$ represents the input optical field incident on the plane of the rotating ground-glass plate, $R_0(x_0, y_0)$, which fluctuates randomly over time, O_1 represents the object at plane (x_1, y_1) , and $\Gamma_1(x_1, x_0, y_1, y_0, z_1)$ is a transmission function from the initial plane (x_0, y_0) to another plane (x_1, y_1) with a distance of z_1 , i.e.,

$$\Gamma_1 = \frac{e^{-ikz_1}}{i\lambda z_1} \exp\left\{\frac{-ik}{2z_1} [(x_0 - x_1)^2 + (y_0 - y_1)^2]\right\}, \quad (3)$$

with k being $2\pi/\lambda$ and λ being the wavelength. $\Gamma_2(x_1, x_s, y_1, y_s, z_2)$ and $\Gamma_3(x_0, x_r, y_0, y_r, z_3)$ are in a form similar to Eq. (3). Then we have

$$\begin{aligned} \langle U_r^* U_s \rangle &= \iiint \iiint dx_0 dy_0 dx'_0 dy'_0 dx_1 dy_1 U_0^* U_0 \\ &\quad \times \langle R_0(x_0, y_0) R_0^*(x'_0, y'_0) \rangle O_1(x_1, y_1) \Gamma_1 \Gamma_2 \Gamma_3^* \\ &= \iiint \iiint dx_0 dy_0 dx'_0 dy'_0 dx_1 dy_1 U_0^*(x'_0, y'_0) \\ &\quad U_0(x_0, y_0) \\ &\quad \times |R_0(x_0, y_0)|^2 \delta(x_0 - x'_0, y_0 - y'_0) \\ &\quad O_1(x_1, y_1) \Gamma_1 \Gamma_2 \Gamma_3^* \\ &= \iiint \iiint dx_0 dy_0 dx_1 dy_1 |U_0(x_0, y_0)|^2 |R_0(x_0, y_0)|^2 \\ &\quad O_1(x_1, y_1) \Gamma_1 \Gamma_2 \Gamma_3^*, \end{aligned} \quad (4)$$

where $U_0^*(x'_0, y'_0)$ is the complex conjugate of $U_0(x_0, y_0)$, δ represents the spatial impulse-response function, and $|U_0(x_0, y_0)|^2 |R_0(x_0, y_0)|^2$ is simplified to a complex constant here.

The propagation process in Fig. 1(b) can be expressed as

$$\begin{aligned} U_r(x_r, y_r) &= \iiint \iiint \Gamma_2(x_1, x_s, y_1, y_s, z_2) O_1(x_1, y_1) \\ &\quad \times \Gamma_1(x_0, x_1, y_0, y_1, z_1) \Gamma_3^*(x_r, x_0, y_r, y_0, z_3) \\ &\quad dx_0 dy_0 dx_1 dy_1. \end{aligned} \quad (5)$$

From comparison of Eqs. (4) and (5), the equivalence between Fig. 1(a) and Fig. 1(b) can be initially proved as

$$G^{(2)} = |\langle U_r^* U_s \rangle|^2 \propto |U_r'(x_r, y_r)|^2, \quad (6)$$

where $G^{(2)}$ represents the second-order correlation function between a point (x_s, y_s) in the signal arm and reference arm's information U_r , termed "forward correlation" here, especially compared with another term, "backward correlation" or "reversed correlation," which is established between point (x_r, y_r) in the reference arm and signal arm's

information U_s . Similarly, the backward second-order correlation function $G_b^{(2)}$ can be expressed as

$$G_b^{(2)} \propto |U_s'(x_s, y_s)|^2, \quad (7)$$

where $U_s'(x_s, y_s)$ represents the propagation process from point source (x_r, y_r) in the reference arm to the phase-conjugate mirror, object, and detection plane in turn. Hence, $U_s'(x_s, y_s)$ can be expressed as

$$\begin{aligned} U_s'(x_s, y_s) &= \iiint \iiint [\Gamma_3(x_0, x_r, y_0, y_r, z_3)]^* \\ &\quad \Gamma_1(x_1, x_0, y_1, y_0, z_1) \\ &\quad \times O_1(x_1, y_1) \Gamma_2(x_s, x_1, y_s, y_1, z_2) dx_0 dy_0 dx_1 dy_1. \end{aligned} \quad (8)$$

From comparison of Eqs. (5) and (8), it can be found that $G^{(2)}$ is a conjugate image of $G_b^{(2)}$. Also, Eqs. (5) and (8) both indicate that the second-order coherence function in the spatial domain has a form similar to the one in the temporal domain as the Siegert relation points out.

The diffraction pattern can be recovered for an amplitude-only object (e.g., a double slit) by means of an autocorrelation operation between a fixed point (x'_s, y'_s) and all points (x_s, y_s) in the signal arm. The reason why any signal arm's autocorrelation $G_{\text{auto}}^{(2)}$, $G_{\text{auto}}^{(2)} = |\langle U_s U_s(x'_s, y'_s)^* \rangle|^2$, fails to retrieve the diffraction pattern of a pure phase object can be expressed as

$$\begin{aligned} \langle U_s U_s(x'_s, y'_s)^* \rangle &= \\ &\quad \iint \exp\left\{\frac{ik}{z_1} [(x'_s - x_s)x_1 + (y'_s - y_s)y_1]\right\} \\ &\quad \times |O_1(x_1, y_1)|^2 dx_1 dy_1 C_0 \\ &\quad \exp\left\{\frac{ik}{2z_1} [(x_s^2 - x_s'^2) + (y_s^2 - y_s'^2)]\right\}, \end{aligned} \quad (9)$$

compared with a cross-correlation function in GD; i.e., Eq. (4) can be further rewritten as

$$\begin{aligned} \langle U_r^* U_s \rangle &= \frac{C_0 k}{i2\pi} \sqrt{\frac{ik}{2\pi z_1 z_2 z_3}} \exp[ik(z_1 + z_2 - z_3)] \\ &\quad \times \iiint \iiint dx_0 dy_0 dx_1 dy_1 O_1(x_1, y_1) \\ &\quad \exp\left(\frac{ik}{2} \times E\right), \\ E &= \frac{(x_s - x_1)^2}{z_2} + \frac{(x_1 - x_0)^2}{z_1} - \frac{(x_r - x_0)^2}{z_3} \\ &\quad + \frac{(y_s - y_1)^2}{z_2} + \frac{(y_1 - y_0)^2}{z_1} - \frac{(y_r - y_0)^2}{z_3}, \end{aligned} \quad (10)$$

where C_0 is a complex constant. As we can see, a significant difference is that $|O_1(x_1, y_1)|^2$ in the autocorrelation function [Eq. (9)], compared with $O_1(x_1, y_1)$ in the cross-correlation function [Eq. (10)], therefore loses the phase information.

B. Revisiting GD of phase objects

In the previous subsection, we theoretically revisited how GD uses spatially incoherent light to reconstruct the diffraction pattern of the target and tell the differences among three types of correlation measurement (backward, forward, and autocorrelation). Here we showcase GD-based experimental cases of pure phase objects [i.e., helical phase structures $e^{-i\ell\phi}$ with different topological charges ℓ [68,69], also known as imprinting orbital angular momentum (OAM) on light]. The experimental setup is shown in Fig. 3(a), and a reflective phase-only spatial light modulator (SLM; Holoeye, PLUTO-VIS-016) functions as the phase target, in which a forked hologram as shown in Fig. 3(b) that carries an OAM mode ($\ell = +1$) is imprinted. In the actual experiment, to avoid 0-order diffraction, a grating structure is applied in the SLM, and an aperture is used to allow only +1-order diffracted light to pass through. Note that the integration time (approximately 1 ms) of the detector in each realization is much shorter than the coherence time of the pseudothermal light (approximately 100 ms). When the pseudothermal light is input, however, speckles of +1 order and 0 order are still aliased to some extent, which may be a potential noisy interference item. Figures 3(c) and 3(e) [Figs. 3(d) and 3(f)] show a single-shot speckle pattern and the corresponding ensemble average over time in the signal (reference) arm, respectively. Even if a second-order autocorrelation operation [Eq. (9)] in the signal arm is applied, no distinguishable pattern is recovered in Fig. 3(g), not to mention the results in Figs. 3(c)–3(f) showing no valid information, either.

Figures 3(h) and 3(i) show the results of the second-order cross-correlation between the signal arm and the reference arm in two contrary manners, where the cross-correlation in Fig. 3(h) comes from the correlation operation between a single pixel of the signal arm and all accessible pixels of the reference arm [i.e., a conventional setting in GD experiments, Eq. (6)], while the cross-correlation in Fig. 3(i) comes from an exactly reversed setting according to Eq. (7). As we can see, a ring-shaped pattern, akin to the vortex beam carrying the OAM mode $\ell = +1$, appears in both second-order-coherence maps compared with a conventional Gaussian spatial distribution as shown in Figs. 4(a), 4(e), and 4(i) (i.e., $\ell = 0$, and only the grating structure is loaded on the SLM). In addition, we also load different helical phase profiles with single or multiplexed OAM onto the SLM, viz.,

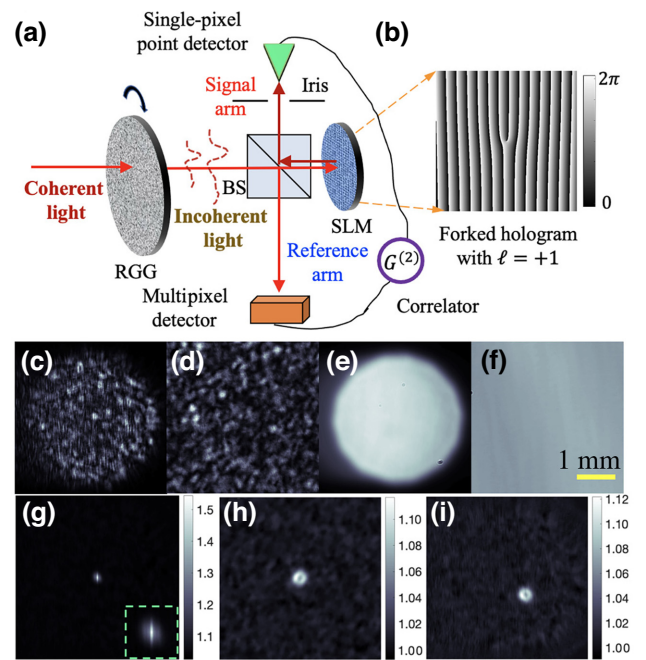


FIG. 3. Observation of the coherent diffraction pattern of a pure phase object with spatially incoherent light. (a) Experimental setup. $z_1 = 5$ cm, $z_2 = 15$ cm, and $z_3 = 20$ cm corresponding to the setup in Fig. 1(a) are set. (b) A pure phase, which is a forked hologram formed by our superimposing a grating and a helical phase structure ($\ell = +1$), is imprinted on a phase-only SLM. (c) [(d)] Single-shot speckle and (e) [(f)] the ensemble average over time of the signal arm (reference arm), respectively. (g) Second-order autocorrelation of the signal arm, where the dotted green frame indicates the enlarged pattern. (h) Forward or (i) backward second-order cross-correlation between the two arms, which can retrieve the diffraction pattern, a ring-shaped intensity profile akin to the vortex beam, whereas none of (c)–(g) can show any phase-object-related information. The scale bar is 1 mm, and 25 000 realizations contribute to the image quality; the same hereinafter for GD²NNs. BS, beam splitter; RGG, rotating ground-glass plate.

$\ell = 0$, $\ell = -2$, $\ell = +1$, -1 , and $\ell = +1$, -2 corresponding to Figs. 4(a)–4(d), respectively. Figures 4(e)–4(h) [Figs. 4(i)–4(l)] show experimental results corresponding to these helical phase profiles obtained with a second-order cross-correlation operation in a forward (backward) manner. It is also noticeable that patterns retrieved in the two manners should have differences according to Eqs. (5) and (8) and the geometrical optics in Fig. 1(b): the forward manner indicates the coherent beam passes through the pure phase object first and then the phase-conjugate mirror, while the backward manner indicates the opposite. Therefore, the forward manner actually obtains the diffraction pattern of the conjugate phase object, so it is also reasonable that the pattern in Fig. 4(h) is exactly inverted compared with the pattern in Fig. 4(l). For a pure amplitude object and some special phase

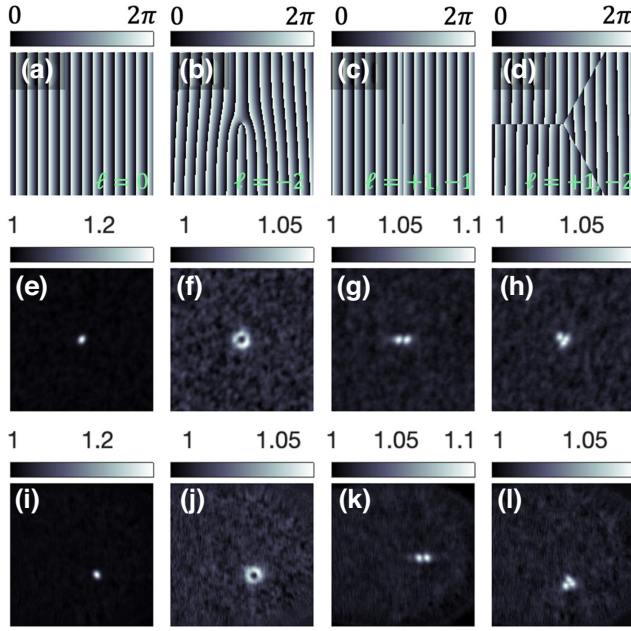


FIG. 4. Experimental results for GD of more pure phase objects with a single or a multiplexed OAM state, viz., (a),(e),(i) $\ell = 0$, (b),(f),(j) $\ell = -2$, (c),(g),(k) $\ell = +1, -1$, and (d),(h),(l) $\ell = +1, -2$. (a)–(d) Phase profiles loaded onto the SLM. (e)–(h) Correlation results in a forward manner. (i)–(l) Correlation results in a backward manner. Notably, these experimental results can be regarded as an approach to designing a second-order correlation function with diverse spatial distributions.

objects [e.g., Figs. 4(a)–4(c), whose diffraction patterns are centrosymmetric], this feature is inconspicuous but crucial in the next section concerning GD²NNs.

III. SORTING WITH GD²NNs

In the previous section, we theoretically and experimentally verified the robustness of using GD to “see” the diffraction patterns of single-layer phase targets with spatially incoherent light. In this section, we show such a phase-conjugate-mirror model is still valid for cascaded or volume phase targets, whereby we transform coherent beam-demanded D²NNs into GD²NNs driven by spatially incoherent light. In addition, these diffraction patterns with different ℓ values are shown in Figs. 3 and 4, and in this section, we demonstrate how to classify them using GD²NNs in a nonlocal fashion.

A. Principle of GD²NNs

First, we briefly introduce the general framework and training flow of D²NNs [41]. Figure 5 depicts three cases of D²NNs: D²NNs with coherent light, D²NNs with spatially incoherent light, and GD²NNs with spatially incoherent light in a nonlocal fashion. In Fig. 5(a) (case 1), a typical N -layer D²NN consists of stratified 2D DOEs,

and a given input coherent light field $u^0(x, y)$ propagates a certain distance z_a and illuminates one of several M -type phase targets $t_p(x, y)$ ($p = 1, 2, \dots, M$), and then the beam passes through each DOE consisting of n diffractive units (viewed as optical neurons) successively and reaches the detection plane as output field $u^{\text{out}}(x, y)$. Considering the unit size of the target and the DOE is much larger than the wavelength in the visible spectrum (e.g., $\lambda = 632.8$ nm), the complex transmittance function of the target and the k th ($k = 1, 2, \dots, N$) thin DOE can be expressed as

$$t^p(x, y) = |A^t| \exp[j\psi^p(x, y)], \quad (11)$$

$$h^k(x, y) = |A^h| \exp[j\phi^k(x, y)], \quad (12)$$

respectively, where $j = \sqrt{-1}$. Note that phase-only modulation is considered to achieve maximum diffraction efficiency in this work, so the amplitude $A^t = A^h = 1$ ideally. According to the Rayleigh-Sommerfeld diffraction equation, each unit of the phase target or DOE can be considered as a secondary source of a wave composed of the following optical mode [41,67] similar to the transmission function Γ in Eq. (3):

$$w_i(x, y, z) = \frac{z}{r^2} \left(\frac{1}{2\pi r} + \frac{1}{j\lambda} \right) \exp\left(\frac{j2\pi r}{\lambda}\right), \quad (13)$$

where z denotes the free-space propagation distance between two planes, the subscript i represents the location (x_i, y_i) of the initial plane, and $r = \sqrt{(x - x_i)^2 + (y - y_i)^2 + z^2}$. Hence, the propagation between any two planes can be well described. For example, the propagation between u^k located at the k th layer and $u^{k+1}(x, y)$ located at the $(k + 1)$ th layer can be expressed as

$$u^{k+1}(x, y) = \sum_{i=1}^n u_i^k h_i^k w_i(x, y, d_k), \quad (14)$$

where d_k denotes the interlayer spacing. For simplicity, Eq. (14) can be rewritten in a matrixwise manner as [44,49]

$$\mathbf{U}_{k+1}^p = \mathbf{W}_{d_k} \mathbf{H}_k \mathbf{U}_k^p, \quad (15)$$

where \mathbf{U}_{k+1}^p represents the vectorized output optical field of the k th layer of the network, \mathbf{W}_{d_k} is the diffractive weight matrix, which is fixed for a certain distance, and \mathbf{H}_k denotes the diagonalization of the k th DOE, i.e., $\mathbf{H}_k = \text{diag}(h^k(x, y))$. As a result, the output optical field in case 1 of the forward propagation can be expressed as

$$\mathbf{U}_{\text{out}}^p = \left(\prod_{k=N}^1 \mathbf{W}_{d_k} \mathbf{H}_k \right) \mathbf{U}_{\text{in}}^p, \quad (16)$$

where $\mathbf{U}_{\text{in}}^p = \mathbf{W}_{d_0} \mathbf{T}_p \mathbf{W}_{z_a} \mathbf{U}_0$, where \mathbf{U}_0 is the vectorized complex optical field $u^0(x, y)$ of the coherent beam and \mathbf{T}_p

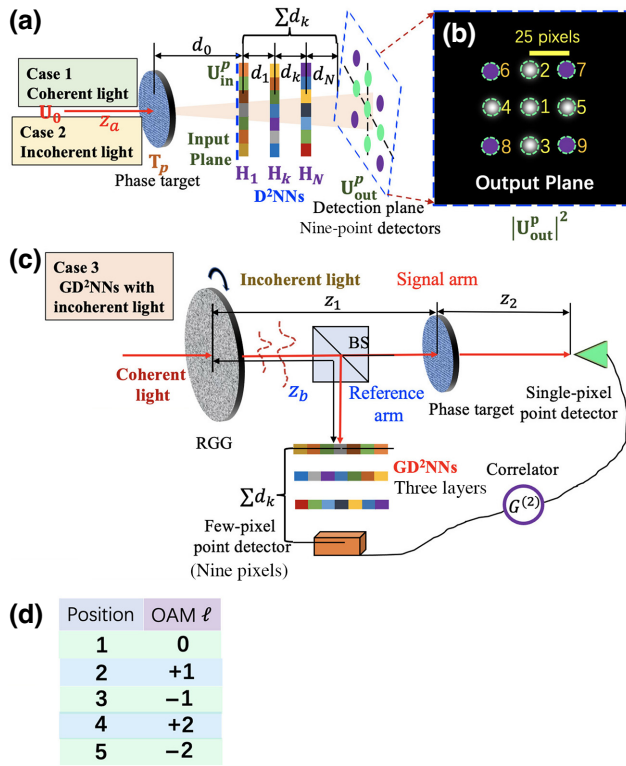


FIG. 5. Three cases of diffractive deep neural networks: case 1, D^2NNs with coherent light; case 2, D^2NNs with spatially incoherent light; case 3, GD^2NNs with spatially incoherent light in a nonlocal fashion. (a) Typical framework of D^2NNs with three layers to realize a mini task, i.e., optical sorting of five types of pure phase target. (b) Detection plane with nine pixels activated: the detectors at positions 1–5 correspond to five different phase targets, and the detectors at positions 6–9 (optional) are used to measure background noise to facilitate subsequent calculation of the signal-to-noise ratio. (c) Typical framework of GD^2NNs . (d) Mapping relationship between the position of the detector and the pure phase targets. BS, beam splitter; RGG, rotating ground-glass plate.

is the diagonalization of $p^p(x, y)$. At the detection plane, only the intensity profile, i.e., $|\mathbf{U}_{out}^p|^2$, is recorded by a few-pixel detector.

Under the condition of monochromatic coherent illumination, the classification index is often used to compare the energy or light-intensity distribution, namely, inputting different types of encoded wave fronts (\mathbf{U}_{in}^p) will focus on different spatial positions on the detection plane ($|\mathbf{U}_{out}^p|^2$) as shown in Fig. 5(b). For a broad-spectrum illumination condition, however, the classification index is used to compare the energy distribution in the spectral domain [48]. Once a specific optical sorting task is initiated, the training of network parameters is essentially an optimization problem. Therefore, a global optimization algorithm, e.g., wave-front matching [57,61,70] and back-propagation [41], is required to train all coefficients in $\{\mathbf{H}_k\}$, including a total

of $n \times N$ neurons, so as to facilitate conversions from given \mathbf{U}_{in}^p to \mathbf{U}_{out}^p with minimum error. See the literature mentioned above for a more-detailed description; this work harnesses mainly the wave-front-matching scheme to train the network. To put it simply, the optimization of phase-only masks is implemented iteratively. In each iteration, there will be $N + 1$ steps. Initially, all layers are set to be randomly or uniformly distributed phase masks, which will be updated in each iteration. For the q th step ($q = 1, 2, \dots, N + 1$) in each iteration, the back-propagating optical field $\widehat{\mathbf{U}}_q^p$, from \mathbf{U}_{out}^p to the q th layer, can be expressed as

$$\widehat{\mathbf{U}}_q^p = \begin{cases} \left(\prod_{k=N+1-q}^1 \mathbf{W}_{d_k}^* \mathbf{H}_k^* \right) (|\mathbf{U}_{out}^p| \odot \mathbf{V}), & q \leq N, \\ |\mathbf{U}_{out}^p| \odot \mathbf{V}, & q = N + 1, \end{cases} \quad (17)$$

where \mathbf{H}_k^* is the complex conjugate of \mathbf{H}_k , $\mathbf{W}_{d_k}^*$ is the complex conjugate of \mathbf{W}_{d_k} representing back-propagating the distance of d_k , \odot denotes elementwise multiplication, and \mathbf{V} is the tentative phase of \mathbf{U}_{out}^p [i.e., $\mathbf{V} = \text{phase}(\mathbf{U}_{out}^p) = \exp[j \arg(\mathbf{U}_{out}^p)]$], initialized by a random vector. Then $\{\mathbf{H}_k\}$ and \mathbf{V} are updated through

$$\begin{aligned} \mathbf{H}_1 &= \text{phase} \left[\sum_{p=1}^M \widehat{\mathbf{U}}_1^p \odot (\mathbf{U}_{in}^p)^* \right], & q = 1, \\ \mathbf{H}_q &= \text{phase} \left[\sum_{p=1}^M \widehat{\mathbf{U}}_q^p \odot (\mathbf{U}_q^p)^* \right], & 1 < q \leq N, \\ \mathbf{V} &= \text{phase}(\mathbf{U}_{out}^p), & q = N + 1. \end{aligned} \quad (18)$$

After a certain number of iterations followed by application of Eqs. (15)–(18), the algorithm will finally converge and the optimized phase-only masks $\{\mathbf{H}_k\}$ are finally obtained. In this way, the well-trained stratified DOEs can function as an optical classifier, and some micromachining techniques can precisely manufacture this classifier. Under coherent illumination, such a classifier can complete the mode conversion of the encoded light to direct maximum energy to the registered spatial location on the detection plane.

For case 2 in Fig. 5(a), i.e., D^2NNs with spatially incoherent light, both the amplitude and the phase of the input optical field \mathbf{U}_0 fluctuate over time, and \mathbf{U}_{in}^p therefore randomly fluctuates, which is equivalent to the input target \mathbf{T}_p being changed over time. So, it is foreseeable that the ensemble average of \mathbf{U}_{out}^p , i.e., $\langle |\mathbf{U}_{out}^p|^2 \rangle$, will not enable optical sorting similar to the result in Fig. 3(e). On the basis of GD, as we showed in the previous section, spatially incoherent light can implement coherent-light-demanded reconstruction of diffraction patterns. Therefore, there is an immediate motivation to combine D^2NNs and GD, as shown in Fig. 5(c) (case 3) as well as Fig. 2(c), where the phase target and the stratified DOEs are placed not successively but far apart in parallel; namely, the phase target

is placed in the signal arm, while the stratified DOEs are placed in the reference arm. A direct but counterintuitive description is that the photons passing through the phase target do not interact with the trained classifier at all in the framework of GD²NNs, but after introduction of a phase-conjugate-mirror-based unfolded analogy as in Fig. 6(a), these nonlocal phenomena can be well interpreted.

It should be noted that the geometrical path is quite different from that of D²NNs in Fig. 5(a) especially for the added phase-conjugate mirror such that the trained classifier cannot be directly applied in GD²NNs. The physical process in Fig. 6(a) and Eqs. (6) and (7) can likewise be written in a matrixwise manner as

$$\mathbf{G}^{(2)} \propto \left| \left(\prod_{k=N}^1 \mathbf{W}_{d_k} \mathbf{H}_k \right) \left[\mathbf{W}_{z_b} (\mathbf{W}_{z_1} \mathbf{T}_p \mathbf{W}_{z_2} \mathbf{U}_0^i)^* \right] \right|^2, \quad (19)$$

where \mathbf{U}_0^i represents the vectorized optical field of an ideal point source and $\mathbf{G}^{(2)}$ denotes the vectorized second-order correlation function $G^{(2)}$ between the reference arm and a point in the signal arm. Compared with Eq. (16), only \mathbf{U}_{in}^p is changed actually. Therefore, in principle, the training flow of GD²NNs should be the same as that of D²NNs, and only the input phase targets need to be re-encoded or corrected according to geometrical parameters for a given GD setup (a specific example is given in Fig. 6). When it comes to actual experimental measurements, the classification index is no longer the first-order light intensity (or energy distribution), $\langle I_s(\mathbf{r}_s^p) \rangle$, but is the second-order-correlation-coefficient $g^{(2)}(\mathbf{r}^p)$ distribution shown in Eq. (1), where \mathbf{r}^p represents the registered spatial location of a certain region [e.g., Figs. 5(b) and 5(d)] on the few-pixel-detector plane.

B. Numerical results

Here, we first demonstrate a mini numerical example, i.e., to classify five pure phase targets carrying OAM modes ℓ from -2 to $+2$ as shown in Fig. 6(b) with a three-layer network ($N = 3$), with each DOE consisting of 256×256 neurons. Figure 5(a) shows a schematic diagram of original D²NNs with coherent (case 1) and incoherent (case 2) light, and in principle, a focus will appear at a certain position of the detection plane [Fig. 5(b)] after the phase target interacts with the well-trained D²NNs. Figure 5(c) shows a schematic diagram of GD²NNs. Specifically, positions 1–5 correspond to $\ell = 0$, $\ell = +1$, $\ell = -1$, $\ell = +2$, and $\ell = -2$, respectively [the mapping table is shown in Fig. 5(d)], while positions 6–9 (optional) represent the background item as a comparison, so theoretically a location-matched nine-pixel detector is enough to facilitate the sorting task by comprehensively judging the light intensity of the first five positions and the last four positions. Figure 6(a) shows the geometrical optics analogy of Fig. 5(c) according to the GD principle, in which the thermal source is replaced by a phase-conjugate mirror. The

five original pure phase targets are displayed in Fig. 6(b), and Fig. 6(c) shows the corresponding recoded pure phase profiles according to the geometrical optics in Fig. 6(a), and therefore these recoded targets are input for training. It is worth noting that Figs. 6(b) and 6(c) just carry the opposite OAM state (i.e., the spiral directions in the two panels are opposite), which is caused by the phase conjugation and was highlighted above. The pixel unit is set as $5.5 \mu\text{m}$, $z_2 = 15 \text{ cm}$, $z_1 = z_b = 25 \text{ cm}$, $d_k = 5 \text{ cm}$ ($k = 1, 2, 3$), and the free-space propagation is numerically computed through a discrete diffraction transform method [71]. It takes about 20 min to implement 100 iterations at a host computer (Intel Core i7, 2.6 GHz, 16 GB) to train three phase-only masks as shown in Fig. 7(a).

A classification example of a pure phase target ($\ell = +2$) is given: Fig. 7(b) shows a cross-section view of the first-order propagation in Fig. 6(a) with trained GD²NNs when the recoded phase target corresponding to $\ell = +2$ in Fig. 6(c) is inserted (case 1). Figures 7(c) and 7(e) [Figs. 7(d) and 7(f)] show a single-shot speckle pattern and the corresponding ensemble average over time in the signal (reference) arm, respectively, neither of which can realize the sorting task for the target and the classifier do not interact physically. Figure 7(g) shows the first-order sorting result for $\ell = +2$ (case 1, coherent illumination), i.e., the intensity profile at the detection plane corresponding to Fig. 7(b). When the spatially incoherent beam is applied directly, however, the original D²NNs will fail as shown in Fig. 7(h) (case 2, incoherent illumination); in this case, the optical sorting task cannot be implemented, whereas the target and the classifier interact directly but ineffectively due to the source's poor spatial coherence. In addition, the second-order autocorrelation of the signal arm [Fig. 7(i)] cannot obtain any information, either, and this phenomenon is similar to Fig. 3(g). When the second-order cross-correlation is used, the result [Fig. 7(j), case 3] shows a prominent bunching effect ($g^{(2)} \approx 1.6 > 1$) located at a certain position corresponding to $\ell = +2$ similarly to case 1 [Fig. 7(g)], confirming that the optical sorting task can be initially achieved with GD²NNs in a nonlocal manner. To be clear, Fig. 7(k) shows acquired temporal light-intensity profiles corresponding to ten positions in the detection planes of the reference and signal arms, respectively, and only the detector at position 4 in the reference arm can exhibit a bunching effect when correlating with the signal arm's detector. Apart from the source, compared with case 1, an additional single-pixel point detector and a beam splitter are needed in case 3. This temporal intensity profile (position 10) corresponding to the signal arm's additional detector thus functions as a key to implement object identification, in which a second-order correlation operation between nine reference-arm intensity profiles and one signal-arm profile is successively, or in parallel, applied to search for the highest bunching correlation coefficient, and

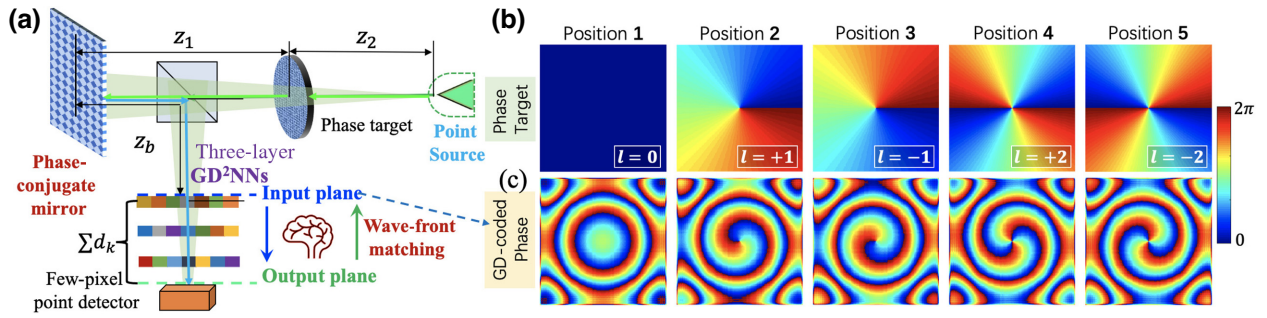


FIG. 6. (a) GD²NNs' unfolded analogy based on the phase-conjugate-mirror model. (b) Five pure phase targets, carrying different OAM modes ℓ from -2 to $+2$, to be classified in a mini optical sorting task. (c) The corresponding recoded input phase targets according to the protocol of the added phase-conjugate mirror and geometrical parameters of the setup.

its spatial location corresponds to a certain type of phase target.

Notably and intriguingly, when the backward second-order cross-correlation is applied, i.e., the correlation between the reference arm's point at position 1 and signal arm's total information, the diffraction pattern of the pure phase target can be obtained as in Fig. 7(l); this phenomenon can be explained likewise using the principle in Fig. 1(b): a point source passes through the GD²NNs, the phase-conjugate mirror, and the phase target, and then reaches the detection plane. According to Figs. 6(b) and 6(c), the backward propagation of the point light source at position 1 corresponds to a beam carrying $\ell = 0$, which will naturally evolve into a vortex beam with $\ell = +2$ after passing through the phase target. In this way, seeing and sorting is facilitated through backward and forward second-order correlation operations, respectively. In Fig. 7(m), all sorting results for the five pure phase targets obtained with GD²NNs are displayed in the second-order-coherence maps.

Concerning the performance or crosstalk possibility, Fig. 8(a) shows the relative energy and second-order-correlation-coefficient distribution matrices for cases 1 and 3. An evaluation index, the signal-to-noise ratio (i.e., SNR), is given by

$$\text{SNR}_{\text{case 1}} = \frac{e_{\text{signal}}}{e_{\text{background}}}, \quad (20)$$

$$\text{SNR}_{\text{case 3}} = \frac{g_{\text{signal}}^{(2)}}{g_{\text{background}}^{(2)}},$$

where $g_{\text{signal}}^{(2)}$ (e_{signal}) and $g_{\text{background}}^{(2)}$ ($e_{\text{background}}$) represent the searched-for maximum at positions 1–5 and the mean of all values other than the maximum in case 3 (case 1), respectively. In the world of second-order coherence, however, the ideal $g_{\text{max}}^{(2)}$ for a thermal source is 2 against $g_{\text{background}}^{(2)} = 1$ generally, so SNR_{max} for case 3 will be less than 2 as $\text{SNR}_{\text{case 3}} = 1.6$, which is much smaller than $\text{SNR}_{\text{case 1}}$, which exceeds 374. It should be clarified that

this comparison is unfair considering background interference or stray light. As shown in Fig. 8(b), the numerical result indicates that $\text{SNR}_{\text{case 1}}$ will decrease rapidly as the relative light-intensity ratio of stray light to signal light increases, which implies that case 1 is much more sensitive to the background interference [also see Eqs. (22) and (23)]. In addition, we also discover that the “untrained” GD²NNs can adaptively identify many other multiplexed holograms carrying two [Figs. 9(a) and 9(b)] or even three [Figs. 9(c) and 9(d)] OAM modes; the term “untrained” means that these additional identification tasks are not optimized at all, i.e., the GD²NNs fed by only the five phase profiles can nevertheless classify the superimposed phase profiles among them. In Fig. 9(e), the second-order-correlation-coefficient distribution matrix, i.e., for sorting two multiplexed phase profiles, is displayed, and shows a reasonable decline in the SNR, being 1.24 compared with 1.6 for sorting a single mode. This feature might result from the orthogonality nature [72] among OAM modes and is beneficial for reducing the complexity of training.

C. Experimental results

In the proof-of-principle experiment, we demonstrate a similar mini optical sorting task for the five pure phase targets carrying OAM modes $\ell = -2$, $\ell = -1$, $\ell = 0$, $\ell = 1$, and $\ell = 2$. We first introduce the experimental realization of two-layer D²NNs as the control group. Figure 10(a) shows the actual framework of the D²NNs, and the phase target is imaged onto the entrance of the two-layer DOEs through a $4f$ system (the focal length and the spacing d_k are both 30 cm). Five labeled locations in the detection plane [Fig. 10(b)] are selected as five output modes, and the mapping relationship between the input OAM modes and the position is shown in Fig. 10(c). The spatial resolution of the DOE is set to 300×300 with a pixel size of $25 \mu\text{m}$, and it takes only approximately 17 min to complete electrical training through 100 iterations as shown in Figs. 10(d) and 10(e). The experimental apparatus shown in Fig. 10(f)

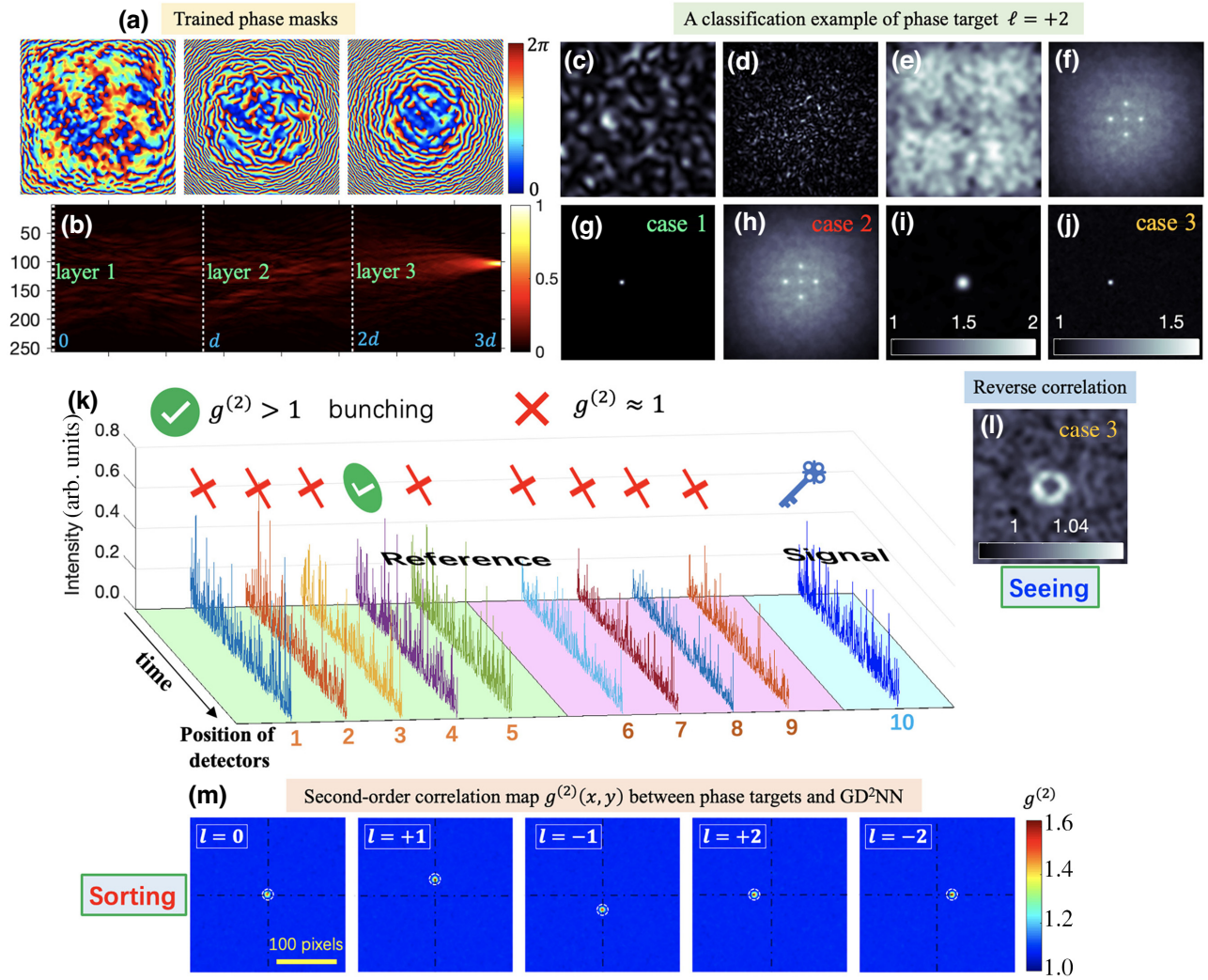


FIG. 7. Results of the mini optical sorting task for five pure phase targets using a three-layer GD^2NN . (a) Three well-trained phase-only DOEs as an optical classifier using Eqs. (15)–(19). A classification example of the pure phase target ($\ell = +2$) is given. (b) Cross-section view of the first-order propagation in Fig. 6(a) with trained GD^2NN s. (c),(d) Single-shot speckle pattern and (e),(f) the ensemble average over time of the signal arm and the reference arm, respectively. Numerical results for first-order optical sorting with (g) spatially coherent light and (h) spatially incoherent light, (i) the signal arm’s second-order autocorrelation, and (j) forward and (l) backward second-order cross-correlation. (k) Ten fluctuating light-intensity profiles in the reference and signal arms. Object recognition cannot be achieved in any single fluctuation but can be achieved in mutual intensity correlation; among the nine positions of interest, only the detector at position 4 produces a positive response, i.e., a distinct bunching effect with second-order correlation coefficient larger than 1, whereas the correlation coefficients of other positions are near 1. (m) All sorting results for five pure phase targets obtained with use of GD^2NN s are shown in their second-order-coherence maps. In this case, notably, seeing and sorting can be facilitated through backward and forward second-order correlation operations, respectively.

follows the structure shown in Fig. 10(a). We use transmissive SLMs (Daheng Optics, GCI-770104, 768×1024 pixels) with a pixel pitch of $12.5 \mu\text{m}$ to realize phase-only modulation, in which the phase functions are encoded into holograms on the basis of the principle of off-axis holography [73–76]; an area of 600×600 pixels (2×2 pixels are composed into a macro pixel) in the center of the SLMs is activated to load these holograms; the iris in Fig. 10(f) is used to allow only the $+1$ -order diffracted light

to pass through, and the free-space propagation of 30 cm also allows the spatial separation of 0-order and $+1$ -order diffracted light. In this regard, although the phase modulation depth of the transmissive SLM is only about half the range ($0-\pi$), arbitrary full-range phase and even complex-amplitude modulation can be achieved with high fidelity through the encoded hologram while avoiding 0-order light interference. After strictly aligning the three SLMs, we load the holograms corresponding to the two-layer phase

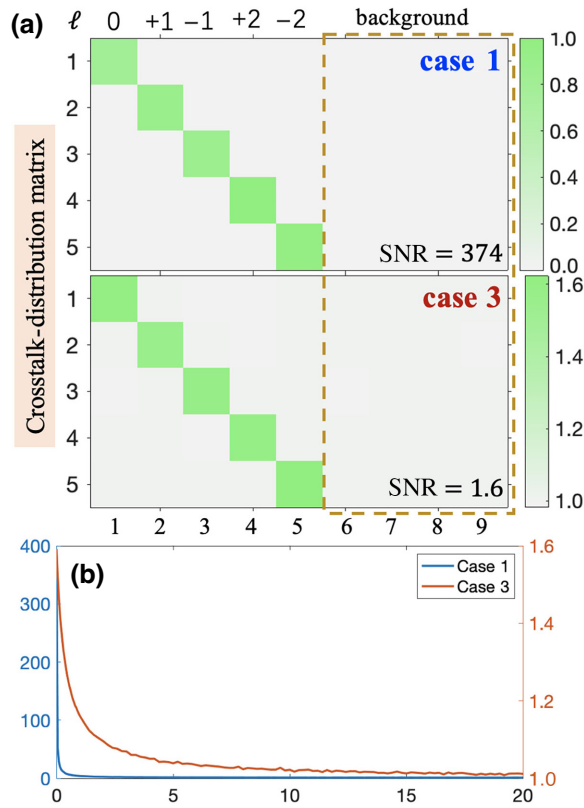


FIG. 8. (a) Correlation strength or $g^{(2)}(\mathbf{r}^p)$ -distribution matrices for cases 1 and 3. The abscissa and ordinate indicate the detector region and the type of input phase profile, respectively. (b) A simple comparison between case 1 and case 3 when the background interference is introduced. The abscissa and ordinate indicate the relative light-intensity ratio of stray light to signal light and the SNR for the two cases, respectively.

functions on SLM2 and SLM3, respectively, and sequentially loaded seven different OAM modes (including five basic modes and two superimposed modes) on SLM1. Under direct irradiation with He-Ne-laser light (632.8 nm) with a beam diameter of approximately 1.8 mm, a CMOS-based image sensor captures the resultant radiance distribution as shown in Figs. 10(g)–10(m) when different modes are input. These recognition results confirm the feasibility of D²NNs under coherent illumination. For spatially incoherent light (e.g., pseudo-thermal light), the detection plane presents only a trivial Gaussian profile as shown in Figs. 10(m)–10(t) regardless of the input of any phase target, such that D²NN-based optical classification will fail as predicted by theory and simulation.

The experimental setup of the two-layer GD²NNs ($N = 2$) is shown in Fig. 11(a). The pseudo-thermal light is divided into two copies by the beam splitter: one beam (signal arm) propagates 15 cm, passes through the phase target (SLM1), and then propagates 60 cm to reach a single-point detector, while the other beam (reference arm) symmetrically propagates 15 cm and passes through two

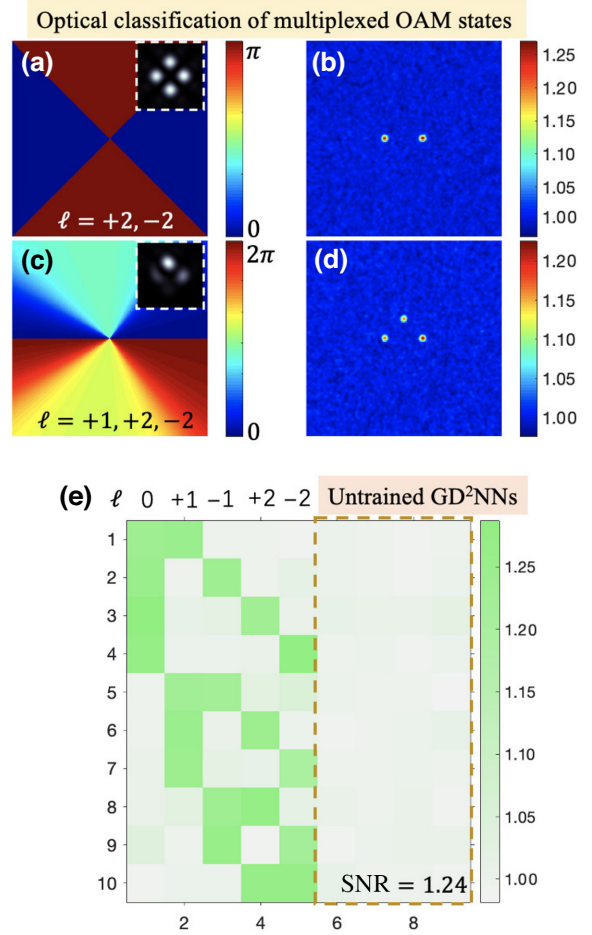


FIG. 9. Optical sorting of multiplexed phase profiles carrying multiple OAM states using the “untrained” GD²NNs fed by the original five phase targets. (a),(c) Superimposed pure phase targets of two and three modes, respectively. The insets correspond to first-order diffraction patterns. (b),(d) Corresponding sorting results for forward second-order cross-correlation operations. (e) $g^{(2)}(\mathbf{r}^p)$ -distribution matrix, which represents the sorting task for two multiplexed modes (a total of ten types) using the identical “untrained” GD²NNs.

cascaded DOEs (SLM2 and SLM3, the spacing d_k is 30 cm and the various parameters are the same as the ones in the D²NNs mentioned above for a fair comparison) before reaching the detection plane. According to the experimental measurement of the geometrical setup, various parameters of the GD²NNs are therefore determined in the unfolded setup shown in Fig. 11(b). Figures 11(c) and 11(d), respectively, show the mapping table and the detection plane with five regions activated, identical to Fig. 10(b). After these parameters have been entered, the training flow is similar to that in the previous subsection using Eqs. (15)–(19). The only difference is that we have increased the diversity of phase types to increase the robustness of the possible position shifts in the light path. For each type of phase target, specifically, multiple

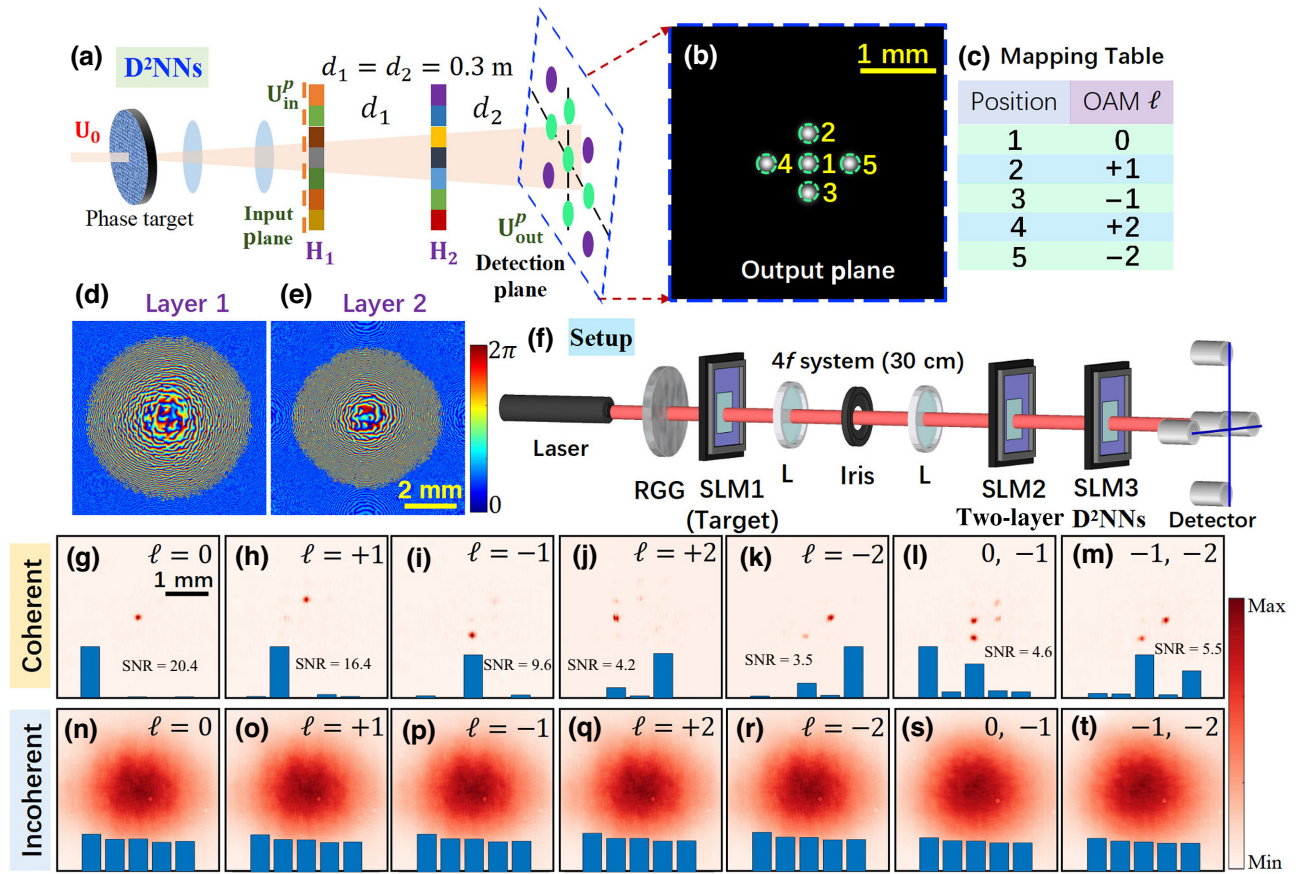


FIG. 10. Experimental realizations of D^2NNs under coherent and spatially incoherent illumination. (a) Actual framework of the two-layer D^2NNs to be trained to classify five types of target. (b) Detection plane with five regions activated as output modes marked with different labels in yellow. (c) Mapping table between different input OAM modes and positions of the output Gaussian modes. (d),(e) Well-trained phase-only masks (300×300 pixels). (f) Experimental apparatus. Experimental classification results for five single OAM modes and two multiplexed OAM modes (g)–(m) with laser light and (n)–(t) with pseudothermal light. The energy distribution corresponding to the five locations is plotted at the bottom in (g)–(t). L, lens; RGG, rotating ground-glass plate.

subsets with a two-pixel offset ($50 \mu\text{m}$) in every direction are added for training, i.e., ten subsets are included for each type ($M = 5 \times 10$). In this way, it takes about 24 min to train the two-layer GD^2NNs after 100 iterations; the phase profiles are shown in Figs. 11(e) and 11(f). It should be noted that only some of the neurons in the second layer are effectively trained due to the noncompact network structure with limited hardware.

Then, the five phase targets from $\ell = -2$ to $\ell + 2$ are loaded on SLM1 in turn, while the well-trained two-layer phase-only masks are loaded on SLM2 and SLM3, and the other settings are similar to those for Fig. 3(a). Experimental results for GD^2NNs are shown in Figs. 11(g)–11(m): when different phase targets are added in the signal arm, the weak bunching effect will appear in different certain positions on the second-order-coherence map, and each correlation function is retrieved with 25 000 realizations. Although the SNR is relatively low compared with the SNR in the simulation reported in the previous subsection,

it is still feasible to classify the multiplexed OAM modes in Figs. 11(l) and 11(m) similar to the classification results in Fig. 9. We show the confusion matrices of D^2NNs in Figs. 12(a) and 12(b) and the $g^{(2)}$ -distribution matrix of GD^2NNs in Fig. 12(c). From coherent to spatially incoherent light, the SNR of D^2NNs suddenly drops from 10.8 to less than 1, making it completely unrecognizable. By use of second-order coherence instead of first-order light intensity, GD^2NNs can initially achieve coherent phase-target classification albeit with a relatively lower SNR of only 1.18. We emphasize that improving the spatial coherence of the light sources can indeed improve the performance of D^2NNs , but it will conversely degrade the performance of GD^2NNs considering the complementarity between coherence and correlation [77]. A large number of realizations ensures the reconstruction of clear correlation patterns, but for classification purposes only, many fewer realizations are possible. Figure 12(d) shows the correlation coefficient as a function of the number of realizations in the case of

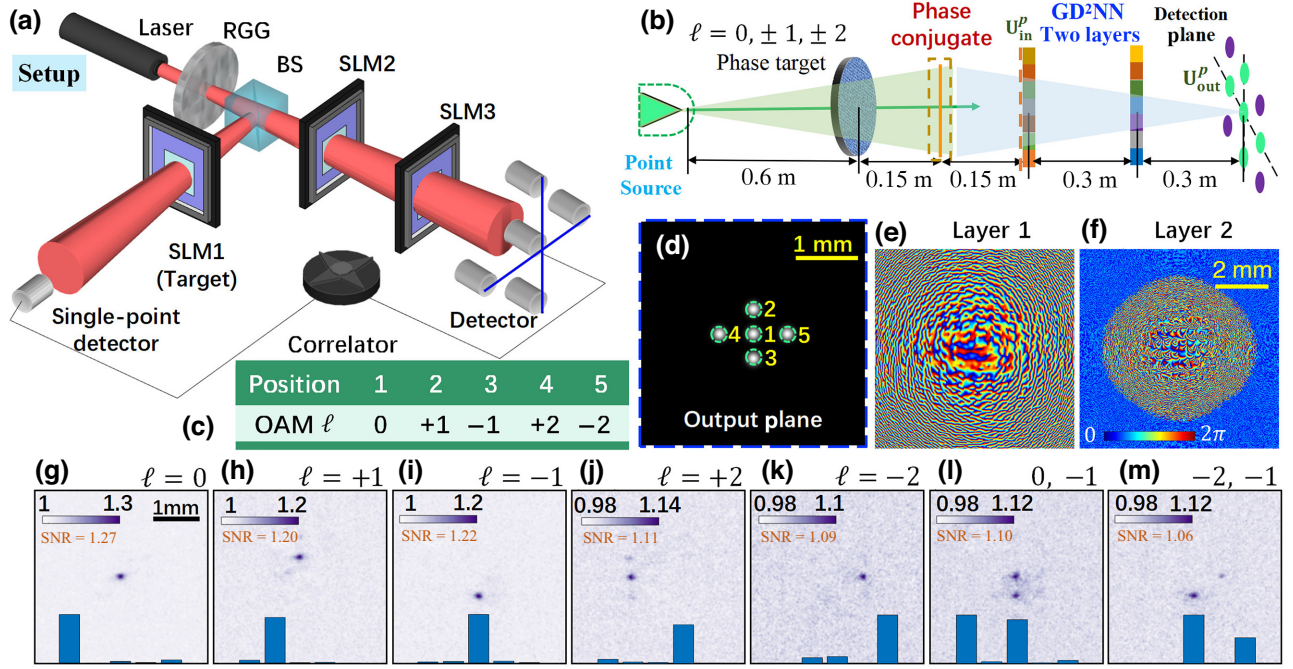


FIG. 11. Experimental demonstration of GD²NNs. (a) Experimental setup including transmissive SLM-enabled two-layer GD²NNs. (b) Unfolded analogy of (a) for training. (c) Mapping relationship. (d) Detection plane with five regions activated identical to Fig. 10(b). (e),(f) Well-trained two-layer phase-only masks (300 × 300 pixels) that are loaded on SLM2 and SLM3, respectively. (g)–(m) Experimental results for the second-order-coherence maps of seven phase targets (SLM1); when different phase targets are added in the signal arm, the bunching effect will appear in different certain positions on the second-order-coherence map. Twenty-five-thousand realizations contribute to the image quality. BS, beam splitter; RGG, rotating ground-glass plate.

$\ell = -2$, where the calculation of the error range is based on nonrepeated grouping from 25 000 samples. When the lowest value in the error range of the correlation coefficient is higher than the highest value in the background's error range, it can be considered that robust recognition can be achieved. Therefore, according to Fig. 12(d), when the number of realizations exceeds 1000, GD²NNs can provide a reliable classification result [Fig. 12(e)]. In processing some lightweight phase-target classification, the results at this stage are acceptable considering that only two-layer networks are used. Besides, ways to further improve the performance of GD²NNs in the future include increasing the number of neurons [46] (i.e., number of layers and the density of each layer), a more-compact network structure (e.g., using stacked metasurfaces [45] instead of SLMs), and high-order correlation operation [78] boosting the correlation coefficient to much greater than 2.

IV. DISCUSSION

A. Extension to GD²NNs with entangled photon pairs

Since the D²NNs have been demonstrated using a classical thermal source, extension to a quantum source should also be feasible according to Klyshko's advanced-wave interpretation [3,4] regarding the source as a mirror. In this

case, Eq. (19) can be rewritten as

$$\mathbf{G}_q^{(2)} \propto \left| \left(\prod_{k=N}^1 \mathbf{w}_{d_k} \mathbf{H}_k \right) [\mathbf{w}_{z_b} \mathbf{w}_{z_1} \mathbf{T}_p \mathbf{w}_{z_2} \mathbf{U}_0^i] \right|^2. \quad (21)$$

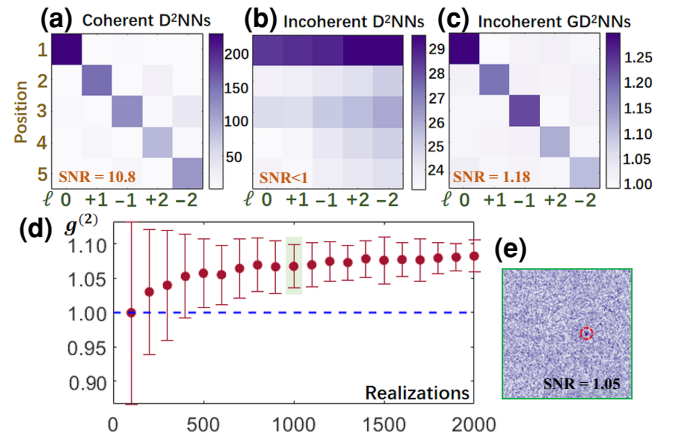


FIG. 12. Confusion matrices (energy-distribution matrices) of D²NNs (a) with coherent light and (b) with pseudothermal light. (c) $g^{(2)}(\mathbf{r}^p)$ -distribution matrix of GD²NNs with pseudothermal light. (d) Correlation coefficient versus the number of realizations in the case of $\ell = -2$. (e) Correlated pattern of $\ell = -2$ when the number of realizations is only 1000.

Other training procedures should be the same as for with the classical GD²NNs mentioned above.

B. Comparisons between D²NNs and GD²NNs

The motivation for proposing GD²NNs is not to improve the classification performance of D²NNs but to fundamentally remove the strict requirements of D²NNs for spatial coherence of light sources. Apart from the obvious differences, which were highlighted in Sec. I and Fig. 2, GD²NNs inherit some other characteristics from correlation-assisted metrologies. Here we qualitatively compare GD²NNs with D²NNs and highlight the potential advantages of GD²NNs and inevitable trade-offs at this stage.

1. Encrypted optical classification

One of the most-intriguing features revealed by GD²NNs is the unique parallel or nonlocal framework distinguished from all reported optical classification frameworks. As illustrated in Fig. 7(k), we note again that any single-arm information cannot complete the classification task, and only the joint measurement is valid. This feature is akin to the ghost-imaging-based optical encryption scheme [79,80] with one arm being the key and the other being the ciphertext; the safety performance is guaranteed by the unpredictable randomness of the thermal source itself, which is not equipped in the D²NNs.

2. Robustness with regard to noise

Distinguished from D²NNs, which exploit the spatial distribution or the spectral content of the first-order light intensity, GD²NNs essentially fully exploit light's second-order coherence as the classification index. The classification performance (such as SNR) of GD²NNs is not as good as that of D²NNs according to Fig. 8, but it may be more advantageous in a strong-stray-light environment (see Refs. [81–83] for more cases).

To be more explicit, considering added noisy light I_n in the signal arm, the second-order correlation coefficient $g_a^{(2)}$ in Eq. (1) can be expressed as

$$g_a^{(2)} = \frac{\langle (I_s + I_n) I_r \rangle}{\langle (I_s + I_n) \rangle \langle I_r \rangle} = \frac{\langle I_r I_s \rangle + \langle I_r I_n \rangle}{\langle I_r \rangle \langle I_s \rangle + \langle I_r \rangle \langle I_n \rangle}. \quad (22)$$

Because I_n and I_r are statistically independent, $\langle I_r I_n \rangle$ is equal to $\langle I_r \rangle \langle I_n \rangle$. Considering that $\langle I_n \rangle = c \langle I_s \rangle$, Eq. (22) can be rewritten as

$$g_a^{(2)} = \frac{\langle I_r I_s \rangle + c \langle I_r \rangle \langle I_s \rangle}{(c + 1) \langle I_r \rangle \langle I_s \rangle} = \frac{c + g_{\text{signal}}^{(2)}}{c + 1} > 1. \quad (23)$$

As we can see, a degenerated bunching effect can still be exploited even when $c \gg 1$, i.e., a strong-stray-light case similar to that in Fig. 8(b). Nevertheless, D²NNs that rely

on light intensity as a criterion will face a huge challenge once $c > 1$.

Moreover, the measurement of $g^{(2)}$ is immune to multiplicative noise in the signal arm that is statistically independent of I_s and I_r . In this case, $g_b^{(2)}$ can be expressed as

$$g_b^{(2)} = \frac{\langle I_r I_s I_n \rangle}{\langle I_r \rangle \langle I_s I_n \rangle} = \frac{\langle I_r I_s \rangle \langle I_n \rangle}{\langle I_r \rangle \langle I_s \rangle \langle I_n \rangle} = g_{\text{signal}}^{(2)}. \quad (24)$$

These two anti-interference capabilities, which are not available in D²NNs, will help GD²NNs achieve better performance in various complex environments. Besides, many studies have shown that second-order-correlation-assisted optical applications can resist atmospheric turbulence [84] and cope with low-light protocols [26,85].

3. Trade-offs between spatial coherence and time consumption

As a common challenge in ghost-imaging and diffraction experiments, the joint measurement whether in the quantum case (coincidence counting) or in the classical case (intensity correlation) relies on the ensemble average over time and therefore inevitably requires a large number realizations (e.g., 25 000 realizations in this work). The advantage of noise immunity [Eqs. (22)–(24)] is also based on the ensemble average of a large number of samples. This is obviously a time-consuming process, so GD²NNs at this stage are doomed to be unable to achieve real-time classification at the speed of light with low energy consumption like D²NNs. So, how to use many fewer realizations is an emerging challenge faced by GD²NNs, and strategies such as compressive sensing and deep learning [26] might be alternatives to optimizing this efficiency issue. In general, we can summarize such a trade-off between spatial coherence and time consumption. In addition, use of a thermal source with much shorter coherence time and use of a few-pixel detector instead of the high-resolution image sensor used here can greatly reduce time consumption and potentially achieve optical classification within seconds.

C. Comparisons with ghost-imaging-based classification schemes

Recently, some single-pixel imaging or ghost-imaging-enabled image-free optical classification schemes [86–88] have been proposed, but they are applicable only for amplitude targets at this stage. The principle of single-pixel imaging or ghost imaging can be well explained by a simple matrix multiplication, i.e., $\mathbf{S} = \mathbf{PI}$ [89], which is quite different from Eq. (19) in GD²NNs; Also, ghost imaging uses a single-pixel bucket detection to record the total intensity in the signal arm, and in this process, only images

of amplitude-only objects can be obtained unless an interferometer is used. GD²NNs here can achieve image-free and interferometer-free classification of complex-amplitude targets with use of a single-pixel point detector and a few-pixel detector, which is therefore also suitable for many unusual wavebands especially when a high-resolution detector is expensive or even nonexistent.

In essence, the single-pixel-imaging-based classification scheme still belongs to the type in Fig. 2(a), except that the optical measurement method—the original array sampling—is replaced by single-pixel sampling; hence, irrespective of whether it is image-free or not image-free, the core of these classification schemes still relies on data-driven end-to-end electrical neural networks as well as electrical inference. Our scheme requires only joint correlation measurement without any electrical postprocessing algorithm to achieve classification tasks, so in this regard GD²NNs can be considered as an *all-optical* classification scheme. Furthermore, the internal structures and parameters of electrical neural networks are often like a “black box” [90], while each neuron and layer in GD²NNs can be well interpreted through optical diffraction and volume holography.

Single-pixel-imaging-based classification can often realize real-time optical sorting because of the popularization of high-speed structured illumination devices such as a digital micromirror array and the rapid development of the computational modality. Bromberg *et al.* [36] simultaneously proposed the concepts of computational ghost imaging and computational ghost diffraction in 2009; however, it is a pity that almost no attention was paid to the latter. GD²NNs can, in principle, migrate from classical to computational [40], such that the reference arm can be removed and real-time classification will be possible.

V. CONCLUSION

From recognizing the second-order coherence of light to using it for various applications such as an intensity interferometer, imaging, diffraction, and optical encryption, this work proposes an all-optical classification scheme exploiting spatially incoherent light’s second-order coherence. Starting from GD experiments on pure phase objects, this work further demonstrates a unique optical information processing framework termed “GD²NNs,” combined with principles of both GD and D²NNs, to initially achieve both image-free and interferometer-free optical classification of pure phase targets. Such a nonlocal or parallel framework fundamentally differs from the general “encoder-decoder-detector” structure and therefore indicates no optical interaction between the encoder and the decoder. The demonstration of G²DNNs not only creates new possibilities for optical classification but also provides a paradigm shift for all other diffraction-based optical applications to be registered in a nonlocal fashion.

ACKNOWLEDGMENTS

We acknowledge the support of the National Natural Science Foundation of China (Grants No. 12274037, No. 11735005, No. 11654003, and No. 61675028), the Beijing Normal University Interdisciplinary Research Foundation for First-Year Doctoral Candidates (Grants No. BNUXKJC2119 and No. BNUXKJC2121), and the Interdiscipline Research Funds of Beijing Normal University.

-
- [1] D. V. Strekalov, A. V. Sergienko, D. N. Klyshko, and Y. H. Shih, Observation of two-photon “ghost” interference and diffraction, *Phys. Rev. Lett.* **74**, 3600 (1995).
 - [2] A. V. Belinskii and D. N. Klyshko, Two-photon optics: diffraction, holography, and transformation of two-dimensional signals, *Sov. Phys. JETP* **78**, 259 (1994).
 - [3] D. N. Klyshko, Combine EPR and two-slit experiments: Interference of advanced waves, *Phys. Lett. A* **132**, 299 (1988).
 - [4] T. B. Pittman, D. V. Strekalov, D. N. Klyshko, M. H. Rubin, A. V. Sergienko, and Y. H. Shih, Two-photon geometric optics, *Phys. Rev. A* **53**, 2804 (1996).
 - [5] A. N. Black, E. Giese, B. Braverman, N. Zollo, S. M. Barnett, and R. W. Boyd, Quantum nonlocal aberration cancellation, *Phys. Rev. Lett.* **123**, 143603 (2019).
 - [6] M. F. Z. Arruda, W. C. Soares, S. P. Walborn, D. S. Tasca, A. Kanaan, R. M. de Araújo, and P. S. Ribeiro, Klyshko’s advanced-wave picture in stimulated parametric down-conversion with a spatially structured pump beam, *Phys. Rev. A* **98**, 023850 (2018).
 - [7] X. Qiu, D. Zhang, W. Zhang, and L. Chen, Structured-pump-enabled quantum pattern recognition, *Phys. Rev. Lett.* **122**, 123901 (2019).
 - [8] J. Zhou, S. Liu, H. Qian, Y. Li, H. Luo, S. Wen, Z. Zhou, G. Guo, B. Shi, and Z. Liu, Metasurface enabled quantum edge detection, *Sci. Adv.* **6**, eabc4385 (2020).
 - [9] N. H. Valencia, S. Goel, W. McCutcheon, H. Defienne, and M. Malik, Unscrambling entanglement through a complex medium, *Nat. Phys.* **16**, 1112 (2020).
 - [10] R. S. Bennink, S. J. Bentley, R. W. Boyd, and J. C. Howell, Quantum and classical coincidence imaging, *Phys. Rev. Lett.* **92**, 033601 (2004).
 - [11] A. Gatti, E. Brambilla, M. Bache, and L. A. Lugiato, Ghost imaging with thermal light: comparing entanglement and classical correlation, *Phys. Rev. Lett.* **93**, 093602 (2004).
 - [12] J. Cheng and S. Han, Incoherent coincidence imaging and its applicability in x-ray diffraction, *Phys. Rev. Lett.* **92**, 093903 (2004).
 - [13] Y. J. Cai and S. Y. Zhu, Ghost interference with partially coherent radiation, *Opt. Lett.* **29**, 2716 (2004).
 - [14] J. Xiong, D. Z. Cao, F. Huang, H. G. Li, X. J. Sun, and K. G. Wang, Experimental observation of classical subwavelength interference with a pseudothermal light source, *Phys. Rev. Lett.* **94**, 173601 (2005).
 - [15] Y. H. Zhai, X. H. Chen, D. Zhang, and L. A. Wu, Two-photon interference with true thermal light, *Phys. Rev. A* **72**, 043805 (2005).

- [16] P. A. Moreau, E. Toninelli, T. Gregory, and M. J. Padgett, Ghost imaging using optical correlations, *Laser Photon. Rev.* **12**, 1700143 (2018).
- [17] W. Martienssen and E. Spiller, Coherence and fluctuations in light beams, *Am. J. Phys.* **32**, 919 (1964).
- [18] R. J. Glauber, The quantum theory of optical coherence, *Phys. Rev.* **130**, 2529 (1963).
- [19] M. Bache, D. Magatti, F. Ferri, A. Gatti, E. Brambilla, and L. Lugiato, Coherent imaging of a pure phase object with classical incoherent light, *Phys. Rev. A* **73**, 053802 (2006).
- [20] S. H. Zhang, L. Gao, J. Xiong, L. J. Feng, D. Z. Cao, and K. Wang, Spatial interference: From coherent to incoherent, *Phys. Rev. Lett.* **102**, 073904 (2009).
- [21] A. J. F. Siegert, Radiation laboratory, Massachusetts Institute of Technology, Report No. 465, 1943.
- [22] D. Ferreira, R. Bachelard, W. Guerin, R. Kaiser, and M. Fouché, Connecting field and intensity correlations: The Siegert relation and how to test it, *Am. J. Phys.* **88**, 831 (2020).
- [23] R. Hanbury Brown and R. Q. Twiss, Correlation between photons in two coherent beams of light, *Nature* **177**, 27 (1956).
- [24] R. Hanbury Brown and R. Q. Twiss, A test of a new type of stellar interferometer on Sirius, *Nature* **178**, 1046 (1956).
- [25] J. Hloušek, M. Dudka, I. Straka, and M. Ježek, Accurate detection of arbitrary photon statistics, *Phys. Rev. Lett.* **123**, 153604 (2019).
- [26] C. You, M. A. Quiroz-Juárez, A. Lambert, N. Bhusal, C. Dong, A. Perez-Leija, A. Javaid, R. J. León-Montiel, and O. S. Magaña-Loaiza, Identification of light sources using machine learning, *Appl. Phys. Rev.* **7**, 021404 (2020).
- [27] Y. S. Ihn, Y. Kim, V. Tamma, and Y. H. Kim, Second-order temporal interference with thermal light: Interference beyond the coherence time, *Phys. Rev. Lett.* **119**, 263603 (2017).
- [28] P. Ryczkowski, M. Barbier, A. T. Friberg, J. M. Dudley, and G. Genty, Ghost imaging in the time domain, *Nat. Photon.* **10**, 167 (2016).
- [29] T. Dertinger, R. Colyer, G. Iyer, S. Weiss, and J. Enderlein, Fast, background-free, 3D super-resolution optical fluctuation imaging (SOFI), *Proc. Natl. Acad. Sci. USA* **106**, 22287 (2009).
- [30] D. G. Monticone, K. Katamadze, P. Traina, E. Moreva, J. Forneris, I. Ruo-Berchera, P. Olivero, I. Degiovanni, G. Brida, and M. Genovese, Beating the Abbe diffraction limit in confocal microscopy via nonclassical photon statistics, *Phys. Rev. Lett.* **113**, 143602 (2014).
- [31] D. Z. Cao, J. Xiong, and K. G. Wang, Geometrical optics in correlated imaging systems, *Phys. Rev. A* **71**, 013801(R) (2005).
- [32] G. Scarcelli, V. Berardi, and Y. H. Shih, Phase-conjugate mirror via two-photon thermal light imaging, *Appl. Phys. Lett.* **88**, 061106 (2006).
- [33] S. H. Zhang, S. Gan, J. Xiong, X. Zhang, and K. Wang, Illusion optics in chaotic light, *Phys. Rev. A* **82**, 021804 (2010).
- [34] S. Gan, S. H. Zhang, T. Zhao, J. Xiong, X. Zhang, and K. Wang, Cloaking of a phase object in ghost imaging, *Appl. Phys. Lett.* **98**, 111102 (2011).
- [35] R. Borghi, F. Gori, and M. Santarsiero, Phase and amplitude retrieval in ghost diffraction from field-correlation measurements, *Phys. Rev. Lett.* **96**, 183901 (2006).
- [36] Y. Bromberg, O. Katz, and Y. Silberberg, Ghost imaging with a single detector, *Phys. Rev. A* **79**, 053840 (2009).
- [37] P. Clemente, V. Duran, E. Tajahuerce, and J. Lancis, Single-pixel digital ghost holography, *Phys. Rev. A* **86**, 041803 (2012).
- [38] Z. Tan, H. Yu, R. Lu, R. Zhu, and S. Han, Non-locally coded Fourier-transform ghost imaging, *Opt. Express* **27**, 2937-2948 (2019).
- [39] R. V. Vinu, Z. Chen, R. K. Singh, and J. Pu, Ghost diffraction holographic microscopy, *Optica* **7**, 1697 (2020).
- [40] Z. Ye, W. Hou, J. Zhao, H. B. Wang, and J. Xiong, Computational holographic ghost diffraction, *Opt. Lett.* **48**, 1618-1621 (2023).
- [41] X. Lin, Y. Rivenson, N. T. Yardimci, M. Veli, Y. Luo, M. Jarrahi, and A. Ozcan, All-optical machine learning using diffractive deep neural networks, *Science* **361**, 1004 (2018).
- [42] Y. Luo, D. Mengu, N. T. Yardimci, Y. Rivenson, M. Veli, M. Jarrahi, and A. Ozcan, Design of task-specific optical systems using broadband diffractive neural networks, *Light Sci. Appl.* **8**, 1 (2019).
- [43] T. Yan, J. Wu, T. Zhou, H. Xie, F. Xu, J. Fan, L. Fang, X. Lin, and Q. Dai, Fourier-space diffractive deep neural network, *Phys. Rev. Lett.* **123**, 023901 (2019).
- [44] T. Zhou, L. Fang, T. Yan, J. Wu, Y. Li, J. Fan, H. Wu, X. Lin, and Q. Dai, In situ optical backpropagation training of diffractive optical neural networks, *Photonics Res.* **8**, 940 (2020).
- [45] J. Weng, Y. Ding, C. Hu, X. F. Zhu, B. Liang, J. Yang, and J. Cheng, Meta-neural-network for real-time and passive deep-learning-based object recognition, *Nat. Commun.* **11**, 1 (2020).
- [46] O. Kulce, D. Mengu, Y. Rivenson, and A. Ozcan, All-optical information-processing capacity of diffractive surfaces, *Light Sci. Appl.* **10**, 1 (2021).
- [47] T. Zhou, X. Lin, J. Wu, Y. Chen, H. Xie, Y. Li, J. Fan, H. Wu, L. Fang, and Q. Dai, Large-scale neuromorphic optoelectronic computing with a reconfigurable diffractive processing unit, *Nat. Photon.* **15**, 367 (2021).
- [48] J. Li, D. Mengu, N. T. Yardimci, Y. Luo, X. Li, M. Veli, Y. Rivenson, M. Jarrahi, and A. Ozcan, Spectrally encoded single-pixel machine vision using diffractive networks, *Sci. Adv.* **7**, eabd7690 (2021).
- [49] G. Wetzstein, A. Ozcan, S. Gigan, S. Fan, D. Englund, M. Soljačić, C. Denz, D. A. B. Miller, and D. Psaltis, Inference in artificial intelligence with deep optics and photonics, *Nature* **588**, 39 (2020).
- [50] D. Brady and D. Psaltis, Control of volume holograms, *J. Opt. Soc. Am. A* **9**, 1167 (1992).
- [51] S. Borgsmüller, S. Noehte, C. Dietrich, T. Kresse, and R. Männer, Computer-generated stratified diffractive optical elements, *Appl. Opt.* **42**, 5274 (2003).
- [52] W. Cai, T. J. Reber, and R. Piestun, Computer-generated volume holograms fabricated by femtosecond laser micro-machining, *Opt. Lett.* **31**, 1836 (2006).
- [53] H. Wang and R. Piestun, Dynamic 2D implementation of 3D diffractive optics, *Optica* **5**, 1220 (2018).

- [54] N. K. Fontaine, R. Ryf, H. Chen, D. T. Neilson, K. Kim, and J. Carpenter, Laguerre-Gaussian mode sorter, *Nat. Commun.* **10**, 1 (2019).
- [55] C. Qian, X. Lin, X. Lin, J. Xu, Y. Sun, E. Li, B. Zhang, and H. Chen, Performing optical logic operations by a diffractive neural network, *Light Sci. Appl.* **9**, 1 (2020).
- [56] I. U. Idehenre and M. S. Mills, Multi-directional beam steering using diffractive neural networks, *Opt. Express* **28**, 25915 (2020).
- [57] Y. Gao, S. Jiao, J. Fang, T. Lei, Z. Xie, and X. Yuan, Multiple-image encryption and hiding with an optical diffractive neural network, *Opt. Commun.* **463**, 125476 (2020).
- [58] Z. Huang, P. Wang, J. Liu, W. Xiong, Y. He, J. Xiao, H. Ye, Y. Li, S. Chen, and D. Fan, All-optical signal processing of vortex beams with diffractive deep neural networks, *Phys. Rev. Appl.* **15**, 014037 (2021).
- [59] A. Yolalmaz and E. Yüce, Spectral splitting and concentration of broadband light using neural networks, *APL Photon.* **6**, 046101 (2021).
- [60] M. Veli, D. Mengu, N. T. Yardimci, Y. Luo, J. Li, Y. Rivenston, M. Jarrahi, and A. Ozcan, Terahertz pulse shaping using diffractive surfaces, *Nat. Commun.* **12**, 1 (2021).
- [61] J. Zhang, Z. Ye, J. Yin, L. Lang, and S. Jiao, Polarized deep diffractive neural network for sorting, generation, multiplexing, and de-multiplexing of orbital angular momentum modes, *Opt. Express* **30**, 26728 (2022).
- [62] S. Goel, M. Tyler, F. Zhu, S. Leedumrongwatthanakun, M. Malik, and J. Leach, Simultaneously sorting overlapping quantum states of light, *Phys. Rev. Lett.* **130**, 143602 (2023).
- [63] Y. LeCun, Y. Bengio, and G. Hinton, Deep learning, *Nature* **521**, 436 (2015).
- [64] G. C. Adam, A. Khiat, and T. Prodromakis, Challenges hindering memristive neuromorphic hardware from going mainstream, *Nat. Commun.* **9**, 1 (2018).
- [65] G. Barbastathis, A. Ozcan, and G. Situ, On the use of deep learning for computational imaging, *Optica* **6**, 921 (2019).
- [66] M. S. S. Rahman, X. Yang, J. Li, B. Bai, and A. Ozcan, Universal linear intensity transformations using spatially-incoherent diffractive processors, *Light: Sci. Appl.* **12**, 195 (2023).
- [67] J. W. Goodman, *Introduction to Fourier Optics* (Roberts and Co, Englewood, Colorado, 2005).
- [68] L. Allen, M. W. Beijersbergen, R. J. C. Spreeuw, and J. P. Woerdman, Orbital angular momentum of light and the transformation of Laguerre-Gaussian laser modes, *Phys. Rev. A* **45**, 8185 (1992).
- [69] A. M. Yao and M. J. Padgett, Orbital angular momentum: origins, behavior and applications, *Adv. Opt. Photonics* **3**, 161 (2011).
- [70] T. Hashimoto, T. Saida, I. Ogawa, M. Kohtoku, T. Shibata, and H. Takahashi, Optical circuit design based on a wavefront-matching method, *Opt. Lett.* **30**, 2560-2562 (2005).
- [71] V. Katkovnik, J. Astola, and K. Egiazarian, Discrete diffraction transform for propagation, reconstruction, and design of wavefield distributions, *Appl. Opt.* **47**, 3481 (2008).
- [72] S. Zheng, S. Xu, and D. Fan, Orthogonality of diffractive deep neural network, *Opt. Lett.* **47**, 1798 (2022).
- [73] G. Tricoles, Computer generated holograms: an historical review, *Appl. Opt.* **26**, 4351-4360 (1987).
- [74] J. Harriman, S. Serati, and J. Stockley, in *Optical Trapping and Optical Micromanipulation II*, Vol. 5930 (SPIE, 2005), p. 605.
- [75] T. W. Clark, R. F. Offer, S. Franke-Arnold, A. S. Arnold, and N. Radwell, Comparison of beam generation techniques using a phase only spatial light modulator, *Opt. Express* **24**, 6249 (2016).
- [76] S. Turtaev, I. T. Leite, K. J. Mitchell, M. J. Padgett, D. B. Phillips, and T. Čížmár, Comparison of nematic liquid-crystal and DMD based spatial light modulation in complex photonics, *Opt. Express* **25**, 29874 (2017).
- [77] A. Gatti, M. Bache, D. Magatti, E. Brambilla, F. Ferri, and L. A. Lugiato, Coherent imaging with pseudo-thermal incoherent light, *J. Mod. Opt.* **53**, 739-760 (2006).
- [78] D. Z. Cao, J. Xiong, S. H. Zhang, L. F. Lin, L. Gao, and K. Wang, Enhancing visibility and resolution in N th-order intensity correlation of thermal light, *Appl. Phys. Lett.* **92**, 201102 (2008).
- [79] P. Clemente, V. Durán, E. Tajahuerce, and J. Lancis, Optical encryption based on computational ghost imaging, *Opt. Lett.* **35**, 2391 (2010).
- [80] P. Zheng, Q. Dai, Z. Li, Z. Ye, J. Xiong, H. C. Liu, G. Zheng, and S. Zhang, Metasurface-based key for computational imaging encryption, *Sci. Adv.* **7**, eabg0363 (2021).
- [81] T. Gregory, P. A. Moreau, E. Toninelli, and M. J. Padgett, Imaging through noise with quantum illumination, *Sci. Adv.* **6**, eaay2652 (2020).
- [82] X. Gao, H. Deng, M. Ma, Q. Guan, Q. Sun, W. Si, and X. Zhong, Removing light interference to improve character recognition rate by using single-pixel imaging, *Opt. Laser Eng.* **140**, 106517 (2021).
- [83] T. Zhang, Z. Ye, H. B. Wang, and J. Xiong, Quantum-illumination-inspired active single-pixel imaging with structured illumination, *Appl. Opt.* **60**, 10151 (2021).
- [84] T. A. Smith and Y. Shih, Turbulence-free double-slit interferometer, *Phys. Rev. Lett.* **120**, 063606 (2018).
- [85] A. X. Zhang, Y. H. He, L. A. Wu, L. M. Chen, and B. B. Wang, Tabletop x-ray ghost imaging with ultra-low radiation, *Optica* **5**, 374 (2018).
- [86] S. Ota, R. Horisaki, Y. Kawamura, M. Ugawa, I. Sato, K. Hashimoto, R. Kamesawa, K. Setoyama, S. Yamaguchi, K. Fujiu, K. Waki, and H. Noji, Ghost cytometry, *Science* **360**, 1246 (2018).
- [87] P. Caramazza, A. Bocolini, D. Buschek, M. Hullin, C. F. Higham, R. Henderson, R. Murray-Smith, and D. Faccio, Neural network identification of people hidden from view with a single-pixel, single-photon detector, *Sci. Rep.* **8**, 1 (2018).
- [88] Z. Zhang, X. Li, S. Zheng, M. Yao, G. Zheng, and J. Zhong, Image-free classification of fast-moving objects using “learned” structured illumination and single-pixel detection, *Opt. Express* **28**, 13269 (2020).
- [89] M. P. Edgar, G. M. Gibson, and M. J. Padgett, Principles and prospects for single-pixel imaging, *Nat. Photonics* **13**, 13 (2019).
- [90] D. Castelvetti, Can we open the black box of AI? *Nat. News* **538**, 20 (2016).